Volume 16
Number 30
14 August 2020
Pages 6937–7174

Soft Matter

rsc.li/soft-matter-journal

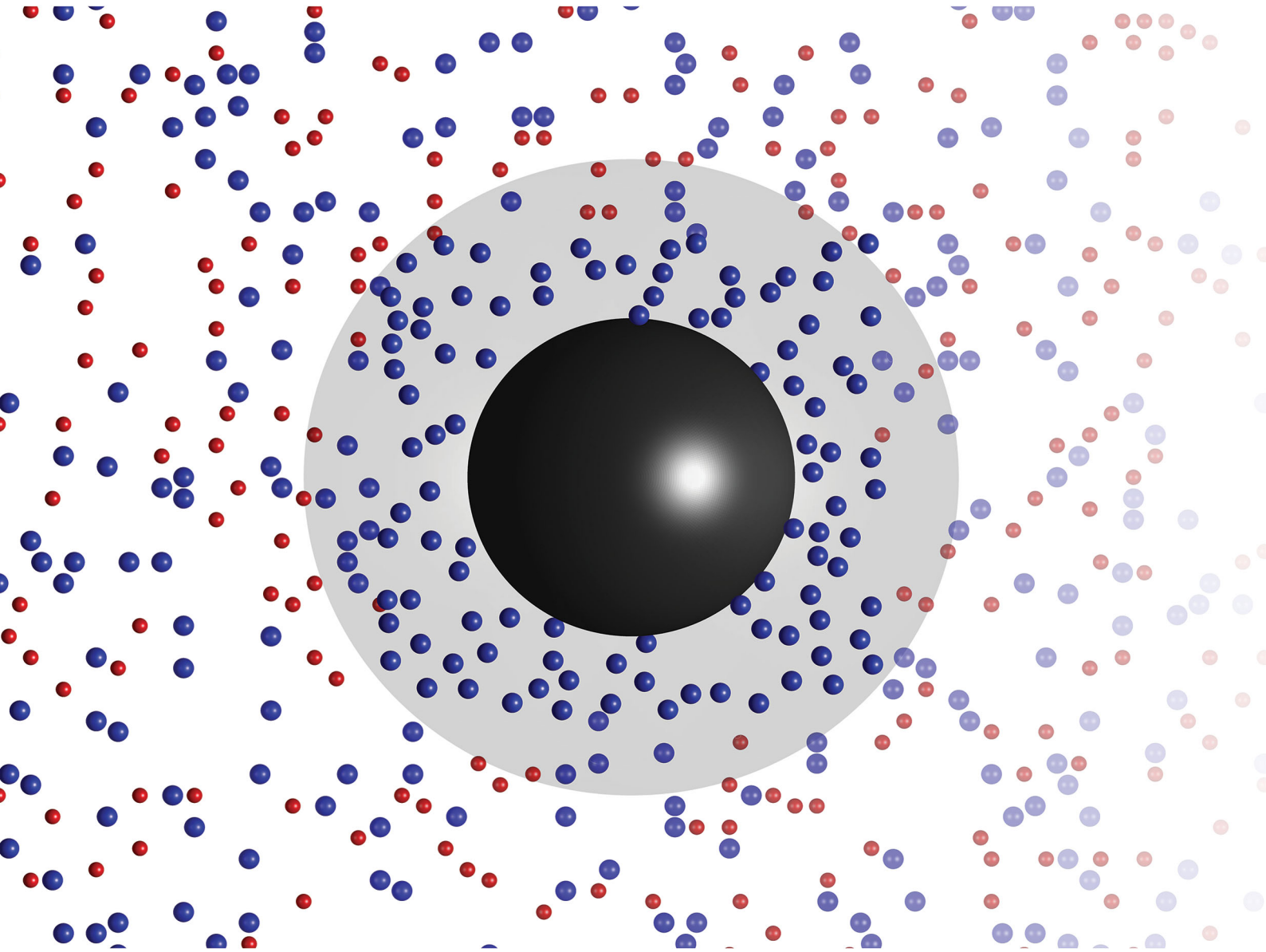

ISSN 1744-6848

ROYAL SOCIETY OF CHEMISTRY

PAPER
Howard A. Stone *et al.*
Diffusiophoresis: from dilute to concentrated electrolytes

Soft Matter

PAPER

View Article Online
View Journal | View Issue

Cite this: *Soft Matter*, 2020, **16**, 6975

Diffusiophoresis: from dilute to concentrated electrolytes

Ankur Gupta, Suin Shim and Howard A. Stone *

Electrolytic diffusiophoresis is the movement of colloidal particles in response to a concentration gradient of an electrolyte. The diffusiophoretic velocity $\mathbf{v}_{DP}$ is typically predicted through the relation $\mathbf{v}_{DP} = D_{DP}\nabla\log c_s$, where D_{DP} is the diffusiophoretic mobility and c_s is the concentration of the electrolyte. The logarithmic dependence of $\mathbf{v}_{DP}$ on c_s may suggest that the strength of diffusiophoretic motion is insensitive to the magnitude of the electrolyte concentration. In this article, we emphasize that D_{DP} is intimately coupled with c_s for all electrolyte concentrations. For dilute electrolytes, the finite double layer thickness effects are significant such that D_{DP} decreases with a decrease in c_s. In contrast, for concentrated electrolytes, charge screening could result in a decrease in D_{DP} with an increase in c_s. Therefore, we predict a maximum in D_{DP} with c_s for moderate electrolyte concentrations. We also show that for typical colloids and electrolytes $\left|\frac{D_{DP}}{D_s}\right| \lesssim 1$, where D_s is the solute ambipolar diffusivity. To validate our model, we conduct microfluidic experiments with a wide range of electrolyte concentrations. The experimental data also reveals a maximum in D_{DP} with c_s, in agreement with our predictions. Our results have important implications in the broad areas of electrokinetics, lab-on-a-chip, active colloidal transport and biophysics.

Received 15th May 2020,
Accepted 3rd July 2020

DOI: 10.1039/d0sm00899k

rsc.li/soft-matter-journal

1 Introduction

The concentration gradient of an electrolyte induces a motion of charged colloidal particles through the phenomenon of diffusiophoresis.[1–6] Since diffusiophoresis enables control of colloidal transport, it has been exploited for applications in active transport,[7–10] membraneless water filtration,[11] zeta potential measurement,[12] delivery or extraction of particles to a dead-end pore,[13,14] colloidal focusing or trapping,[15–17] among others. Fundamental investigations have focused on understanding the effect of surfactant concentration gradients,[18] high salinity,[19] ion valence[20–22] and multiple electrolytes[20,23,24] on the diffusiophoresis of colloidal particles.

In electrolytic diffusiophoresis, the diffusiophoretic velocity $\mathbf{v}_{DP}$ is given by $\mathbf{v}_{DP} = D_{DP}\nabla\log c_s$ (ref. 3), where D_{DP} is the diffusiophoretic mobility and c_s is the electrolyte concentration. This expression has been utilized for a wide variety of experimental and theoretical studies.[10–16,20,22,25–27] Since D_{DP} is typically assumed to be constant, the logarithmic dependence suggests that $\mathbf{v}_{DP}$ is insensitive to the magnitude of electrolyte concentration. For instance, if there are two concentration fields where one varies from 0.01 mM to 1 mM and the other varies from 10 mM to 1 M, and the conditions are such that both the fields have identical $\nabla\log c_s$, the above relation implies that the diffusiophoretic response will remain the same. In fact, in some scenarios, the logarithmic dependence can even predict a ballistic motion of colloidal particles where the particle transport is orders of magnitude faster than the diffusive transport of solute.[25,27] Therefore, in this article, we focus on the assumption that D_{DP} is constant and investigate the impact of a concentration dependent diffusiophoretic mobility, which is consistent with theory for predicting the influence of electrolyte concentration, on the aforementioned predictions.

The principal conclusion of our analysis is that assuming D_{DP} to be constant may lead to inaccurate conclusions since D_{DP} is a strong function of electrolyte concentration c_s. In the dilute limit, the finite double layer thickness effects become significant such that D_{DP} decreases with a decrease in c_s. In contrast, for the concentrated limit, charge screening could become significant[19] and an increase in c_s could result in a lower D_{DP}. Upon inclusion of all these effects, we demonstrate that D_{DP} *versus* c_s displays a maximum for moderate electrolyte concentrations. We calculate achievable D_{DP} values for typical colloids and electrolytes and observe that $\left|\frac{D_{DP}}{D_s}\right| \lesssim 1$, where D_s is the solute ambipolar diffusivity. We validate our predictions through experiments in a dead-end pore configuration where we vary electrolyte concentration by four orders of magnitude, while keeping $\nabla\log c_s$ constant.

Department of Mechanical and Aerospace Engineering, Princeton University, Princeton, NJ 08544, USA. E-mail: hastone@princeton.edu

2 Mathematical details

We consider a binary 1 : 1 electrolyte (*e.g.* NaCl and KCl) where the ion concentration is denoted by $c_s(\mathbf{x},t)$. We assume that the colloidal particles of radius a and concentration n_p are present in a concentration gradient of electrolyte $\nabla c_s(\mathbf{x},t)$ (Fig. 1). The transport of c_s is governed by

$$\frac{\partial c_s}{\partial t} + \nabla \cdot (\mathbf{v}_{fluid} c_s) = D_s \nabla^2 c_s, \tag{1}$$

where $\mathbf{v}_{fluid}$ is the fluid phase velocity and D_s is the electrolyte ambipolar diffusivity.[28,29] For a 1 : 1 electrolyte, $D_s = \frac{2D_+D_-}{D_+ + D_-}$, where D_+ and D_- are diffusivities of the cations and the anions respectively. To describe the conservation of particles, we write

$$\frac{\partial n_p}{\partial t} + \nabla \cdot (\mathbf{v}_p n_p) = D_p \nabla^2 n_p, \tag{2}$$

where $\mathbf{v}_p$ is the particle velocity and D_p is the diffusivity of the particle. The particle velocity is given by[12,16,26,27]

$$\mathbf{v}_p = \mathbf{v}_{DP} + \mathbf{v}_{fluid}, \tag{3}$$

where $\mathbf{v}_{DP}$ is the induced diffusiophoretic velocity and is estimated as[3]

$$\mathbf{v}_{DP} = D_{DP} \nabla \log c_s, \tag{4}$$

where D_{DP} is the diffusiophoretic mobility. Prieve *et al.*[3] showed that for a spherical particle D_{DP} is of the form (for a 1 : 1 electrolyte)

$$D_{DP} = \frac{\varepsilon \left(\frac{k_B T}{e}\right)^2}{\mu} \left(\frac{u_0(\zeta)}{1 - \frac{\lambda}{a} \frac{u_1(\zeta, \mathrm{Pe})}{u_0(\zeta)}} \right), \tag{5}$$

where ε is the electrical permittivity, k_B is the Boltzmann constant, T is temperature, e is the charge on an electron, μ is the fluid phase viscosity, $\lambda = \sqrt{\frac{\varepsilon k_B T}{2e^2 c_s}}$ is the Debye length and ζ is the dimensionless zeta potential scaled by the thermal potential $\frac{k_B T}{e}$. The numerator, *i.e.*, $u_0(\zeta)$ is the leading-order term and is evaluated as[2,3,20]

$$u_0(\zeta) = \beta\zeta + 4 \log\left(\cosh\left(\frac{\zeta}{4}\right)\right), \tag{6}$$

where $\beta = \frac{D_+ - D_-}{D_+ + D_-}$. The first term in eqn (6) is the electrophoretic contribution and the second term is the chemiphoretic contribution. We note that for $|\zeta| \gg 1$, $u_0(\zeta)$ is linear in $|\zeta|$. We also note that $u_0(\zeta)$, and by extension D_{DP}, could be positive or negative,[3,20] *i.e.*, the particle can move up or down the external gradient.

The term in the denominator, *i.e.*, $\frac{u_1(\zeta, \mathrm{Pe})}{u_0(\zeta)}$ is the $O\left(\frac{\lambda}{a}\right)$ correction,[3] where $\mathrm{Pe} = \frac{\varepsilon (k_B T/e)^2}{\mu D_s}$, is the Péclet number. Since the expression of $u_1(\zeta,\mathrm{Pe})$ involves several integral terms and series expansions, we only summarize the main features here and refer the readers to the details provided in the Appendix and ref. 3 (see pp. 266–267, eqn (B1)–(B12)). The value of $u_1(\zeta,\mathrm{Pe})$ is always negative such that the correction typically decreases D_{DP}. More importantly, the correction can become significant even for $\frac{\lambda}{a} \lesssim O(10^{-1})$.[3,14] Finally, the value of $u_1(\zeta,\mathrm{Pe})$ is exponential in $|\zeta|$; see Fig. 5 in ref. 3. We also note that since u_1 is always negative, when u_0 is also negative, eqn (5) may breakdown as $1 - \frac{\lambda}{a}\frac{u_1}{u_0}$ may approach zero. However, the negative value of u_0 is only observed in a very small potential window,[3,20] *i.e.*, when the electrophoretic and chemiphoretic contributions compete with each other. Therefore, eqn (5) will be likely valid in most circumstances. Nonetheless, in this article, we only utilized eqn (5) for $u_0 > 0$, in which limit eqn (5) is always valid.

Depending on the surface chemistry, the dimensionless zeta potential ζ may further depend on c_s. We assume that ζ_{ref} is a reference zeta potential at a specified concentration of the salt c_{ref} such that $\lambda_{ref} = \sqrt{\frac{\varepsilon k_B T}{2e^2 c_{ref}}}$. The commonly described boundary conditions are constant potential (CP) and constant charge (CC). Mathematically, the CP boundary condition reads

$$\zeta = \zeta_{ref}, \tag{7}$$

where the zeta potential is independent of salt concentration. For the CC boundary condition, $q = -\varepsilon \mathbf{n} \cdot \nabla\psi|_{surf}$, where q is the surface charge density, ε is the electrical permittivity, $\mathbf{n}$ is the unit normal vector to the surface and ψ is the electrical potential. The standard Gouy–Chapman solution for isolated surfaces (*i.e.*, dilute suspensions) yields $q = \frac{2\varepsilon k_B T}{e\lambda} \sinh\left(\frac{\zeta}{2}\right)$. Therefore, the CC boundary condition becomes

$$\frac{\lambda_{ref}}{\lambda} \sinh\left(\frac{\zeta}{2}\right) = \sinh\left(\frac{\zeta_{ref}}{2}\right), \tag{8}$$

where the zeta potential increases with a decrease in salt concentration to maintain a constant surface charge. We note

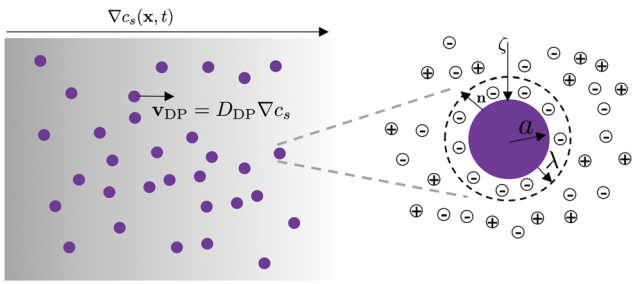

Fig. 1 Colloidal particles of radius a in a solute concentration gradient, *i.e.*, $\nabla c_s(\mathbf{x},t)$. The diffusiophoretic velocity of the particles is given as $\mathbf{v}_{DP} = D_{DP}\nabla \log c_s$. We investigate the effect of finite $\frac{\lambda}{a}$ values and the effect of different surface boundary conditions on D_{DP}.

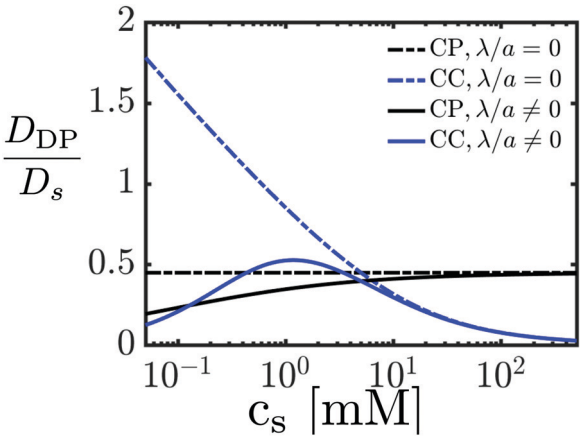

Fig. 2 Dependence of electrolyte concentration c_s on diffusiophoretic mobility D_{DP} as given by eqn (5)–(8). The physical parameters correspond to that of an aqueous NaCl solution, *i.e.*, $D_+ = 1.33 \times 10^{-9}$ m^2 s^{-1}, $D_- = 2.03 \times 10^{-9}$ m^2 s^{-1}, $\varepsilon = 6.9 \times 10^{-10}$ F m^{-1}, $k_B = 1.38 \times 10^{-23}$ J K^{-1}, $T = 298$ K, $e = 1.6 \times 10^{-19}$ C and $\mu = 10^{-3}$ Pa s. In addition, we assume $a = 0.5$ μm, $c_{ref} = 5$ mM and $\zeta_{ref} = -3$. We note that $\frac{\lambda}{a}$ increases as c_s decreases. For the aforementioned physical parameters, $\frac{\lambda}{a} = 6.1 \times 10^{-2}$ for $c_s = 0.1$ mM and $\frac{\lambda}{a} = 1.9 \times 10^{-3}$ for $c_s = 100$ mM.

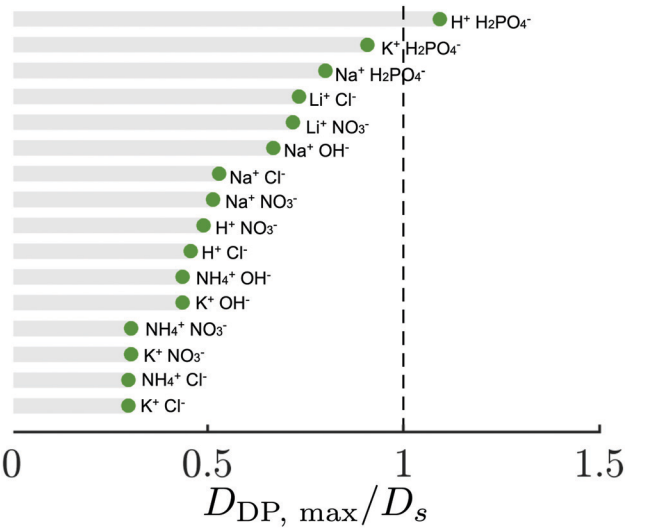

Fig. 3 Summary of maximum $\frac{D_{DP}}{D_s}$ values for 16 different electrolytes based on the constant charge boundary condition and while including finite double layer effects. We adjusted the sign of the zeta potential such that $\beta\zeta > 0$ to ensure that the electrophoretic term and the chemiphoretic term are additive; see eqn (6). We assume $\zeta_{ref} = \pm 3$ (corresponding to ± 75 mV) at $a = 0.5$ μm and $c_{ref} = 5$ mM. The diffusivity values for cations and anions are taken from ref. 2.

that $\frac{\lambda_{ref}}{\lambda} = \sqrt{\frac{c_s}{c_{ref}}}$. Also, we recognize that the Gouy–Chapman solution is the leading order solution for a spherical geometry. The $O\left(\frac{\lambda}{a}\right)$ correction[3] can be included in the expression of q. However, the correction is negligible for typical parameter values and thus has not been included here. Eqn (8) suggests[30] that for $\zeta \ll 1$, $\zeta \propto \frac{\lambda}{\lambda_{ref}}$. For $\zeta \gg 1$, $\zeta \propto \log\left(\frac{\lambda}{\lambda_{ref}}\right)$.

We acknowledge that both the CP and CC are idealized boundary conditions and may not be able to capture the details of the colloidal surface chemistry. Nonetheless, CP and CC boundary conditions help identify the range of diffusiophoretic mobilities to be expected in common experiments. In addition to CC and CP, a charge regulation boundary condition is also employed where the surface charge can include both mobile and immobile charges.[31–34] However, since the charge regulation boundary conditions needs additional parameters, we did not include it in our analysis. Finally, electrical permittivity and viscosity might also be influenced for very concentrated electrolytes[19,21] but these effects haven't been incorporated here since we consider $c_s \lesssim 1$ M.

3 Diffusiophoretic mobility

Using eqn (5)–(8), we summarize the effect of finite double layer thickness and different boundary conditions on D_{DP} in Fig. 2. We utilize the parameter values of an aqueous NaCl solution at room temperature, *i.e.*, $D_+ = 1.33 \times 10^{-9}$ m^2 s^{-1}, $D_- = 2.03 \times 10^{-9}$ m^2 s^{-1}, $\varepsilon = 6.9 \times 10^{-10}$ F m^{-1}, $k_B = 1.38 \times 10^{-23}$ J K^{-1}, $T = 298$ K, $e = 1.6 \times 10^{-19}$ C and $\mu = 10^{-3}$ Pa s. In addition, we assume $a = 0.5$ μm, $c_{ref} = 5$ mM and $\zeta_{ref} = -3$ (*i.e.*, a zeta potential of about -75 mV).[12] The results for the CP boundary condition without including the finite double layer thickness effect $\left(\frac{\lambda}{a} = 0\right)$ predicts a constant D_{DP}, which is the most widely used assumption in the diffusiophoresis literature.[10,12,15–17,22,25–27] The results for the CC boundary condition show a monotonically decaying value of D_{DP} with c_s since the dimensionless ζ potential monotonically decreases with an increase in c_s; see eqn (8). However, when we include the effect of finite double layer thickness, D_{DP} decreases for dilute concentrations for both the CP and CC boundary conditions. In fact, since the value of $\frac{u_1(\zeta, Pe)}{u_0(\zeta)}$ is exponential in $|\zeta|$, the decrease is larger for the CC boundary condition. Therefore, the CC boundary condition with finite double layer effects predicts a maximum in D_{DP} with c_s. We note that the influence of D_{DP} on c_s for the CP boundary condition is through $\frac{\lambda}{a}$ only. In contrast, for the CC boundary condition, the dependence of D_{DP} on c_s is through both $\frac{\lambda}{a}$ and ζ. For the assumed physical parameters, $c_s = 0.1$ mM implies $\frac{\lambda}{a} = 6.1 \times 10^{-2}$. For both the CP and CC boundary conditions, D_{DP} decreases significantly for $c_s = 0.1$ mM even though the value of $\frac{\lambda}{a}$ is significantly smaller than $O(1)$; see Fig. 2. Therefore, finite double layer thickness effects can be significant even for $\frac{\lambda}{a} = O(10^{-2}) - O(10^{-1})$. We reiterate that the surface chemistry of real surfaces might be a combination of the CC and CP boundary conditions which implies that the change in D_{DP} value around the maximum value may

be smaller than the change predicted by the CC boundary condition alone.

For $\frac{\lambda}{a} \neq 0$, we remark that the values of $\left|\frac{D_{DP}}{D_s}\right| \lesssim 1$ for the entire range of c_s; see Fig. 2. This trend is intuitive since the particle motion is induced by solute gradients and the electrolyte establishes D_s. However, some recent reports have utilized $\left|\frac{D_{DP}}{D_s}\right| = O(10) - O(10^3)$.[25,27,35] To make clear typical ranges of diffusiophoretic mobilities in different electrolyte solutions, we seek to verify if $\left|\frac{D_{DP}}{D_s}\right| \lesssim 1$ is applicable to all electrolytes. We summarize the maximum D_{DP} values assuming the CC boundary condition and $\frac{\lambda}{a} \neq 0$ for 16 different binary salts; see Fig. 3. To determine the maximum value of D_{DP} for each electrolyte, we adjusted the sign of the zeta potential such that $\beta\zeta > 0$ to ensure that the electrophoretic term and the chemiphoretic term are additive; see eqn (6). We assumed $\zeta_{ref} = \pm 3$ (corresponding to ± 75 mV) at $a = 0.5$ μm and $c_{ref} = 5$ mM. We note that these are relatively favorable conditions since typical colloidal zeta potentials measured experimentally are lower than ± 75 to ± 100 mV.[36] We find that the majority of the electrolytes still satisfy $\left|\frac{D_{DP}}{D_s}\right| \lesssim 1$. The only electrolyte that displays $\frac{D_{DP}}{D_s} > 1$ is $H^+H_2PO_4^-$; see Fig. 3. However, $H^+H_2PO_4^-$ is likely to be found in aqueous solutions with HPO_4^{2-} and PO_4^{3-} ions when phosphoric acid disassociates. As indicated in Fig. 2, we typically find that the maximum value of D_{DP} is obtained for $c_s = O(1)$ mM, which helps identify the range of concentration values where diffusiophoresis is most effective. We also repeated the analysis assuming different zeta potential values, *i.e.*, $\zeta_{ref} = \pm 4$ (± 100 mV) at $c_{ref} = 5$ mM and obtained similar results where 14 out of the 16 electrolytes showed $\left|\frac{D_{DP}}{D_s}\right| \lesssim 1$, except $K^+H_2PO_4^-$ and $H^+H_2PO_4^-$. We also obtain the same trends with the CP boundary condition; see Fig. 6 in the Appendix. Therefore, $\left|\frac{D_{DP}}{D_s}\right| \lesssim 1$ is likely to be valid for the majority of the electrolytes.

4 Diffusiophoretic response to the spread of a Gaussian solute

We investigate the scenario where colloidal particles respond diffusiophoretically to a constant mass of solute diffusing in space. We assume that the initial distribution of solute is Gaussian with a width of ℓ_0. We consider a one-dimensional problem such that $c_s(x,t)$, $\mathbf{v}_{DP} = v_{DP}\mathbf{e}_x$ and $\mathbf{v}_{fluid} = \mathbf{0}$. We define $X = \frac{x}{\ell_0}$ and $\tau = \frac{D_s t}{\ell_0^2}$. The solution of eqn (1) yields

$$c_s(X,\tau) = \frac{c_0}{\sqrt{1+4\tau}} \exp\left(-\frac{X^2}{1+4\tau}\right), \tag{9}$$

where $c_s(X = 0,\tau = 0) = c_0$. Further, we define the dimensionless velocity $V_{DP} = v_{DP}\ell_0/D_s$. By utilizing eqn (5), we write

$$V_{DP}(X,\tau) = \mathrm{Pe}\left(\frac{u_0(\zeta)}{1 - \frac{\lambda}{a}\frac{u_1(\zeta,\mathrm{Pe})}{u_0(\zeta)}}\right)\frac{\partial}{\partial X}(\log c_s). \tag{10}$$

By using eqn (9) in eqn (10), we obtain

$$V_{DP}(X,\tau) = -2\mathrm{Pe}\left(\frac{u_0(\zeta)}{1 - \frac{\lambda}{a}\frac{u_1(\zeta,\mathrm{Pe})}{u_0(\zeta)}}\right)\frac{X}{1+4\tau}. \tag{11}$$

Assuming $\ell_0 = 1$ mm, $t = 60$ s, $c_0 = 11.8$ mM, $\zeta_{ref} = -3$, $c_{ref} = 5$ mM and using the parameter values that correspond to aqueous solution of NaCl (provided earlier), we report $c_s(X,\tau = 0.1)$ (Fig. 4(a)), $\frac{\lambda}{a}(X,\tau = 0.1)$ (Fig. 4(b)) and $|V_{DP}|(X,\tau = 0.1)$ (Fig. 4(c)) for both constant potential and constant charge boundary conditions. The distribution of c_s shows that the concentration gradient is significant only for $|X| \lesssim 2$ (Fig. 4(a)). The values of $\frac{\lambda}{a}$ can be quite large; see Fig. 4(b). However, the values of V_{DP} are monotonically increasing for $\frac{\lambda}{a} = 0$ models; see eqn (11) and Fig. 4(b). In fact, even for $X = 6$, *i.e.*, the region where solute has not yet diffused, the predictions with $\frac{\lambda}{a} = 0$ suggest that the velocity can be significant. Furthermore, the predictions suggest a ballistic motion for $X = O(10^2)$. Clearly, $\frac{\lambda}{a}$ should not be ignored in this physical system since $\frac{\lambda}{a} \gtrsim O(1-10)$ and even a value of $\frac{\lambda}{a} = 10^{-2} - 10^{-1}$ could significantly influence D_{DP}; see Fig. 2. Therefore, upon inclusion of finite double layer thickness effects, V_{DP} sharply drops beyond $|X| > 2$ (where $\frac{\lambda}{a} \gtrsim O(10^{-1})$), and the ballistic motion vanishes for both CP and CC boundary conditions.

Recently, this particular configuration and its variants have been investigated in detail[25–27] while using the CP boundary condition with $\frac{\lambda}{a} = 0$ and $\left|\frac{D_{DP}}{D_s}\right| = O(1) - O(10^3)$. Specifically, in ref. 25, the authors solved for $n_p(x,t)$ through eqn (2) numerically and demonstrated that for $-\frac{D_{DP}}{D_s} \gg 1$, the variance in $n_p(x,t)$ scales super-linearly with time, a feature the authors described as super-diffusive. We believe that the super-diffusive regime will be challenging to obtain experimentally from diffusiophoresis alone because $\left|\frac{D_{DP}}{D_s}\right| \lesssim 1$. In addition, the finite-double layer effects will significantly reduce the velocity magnitude; see Fig. 4(c). In summary, although the aforementioned studies provide useful insights into the diffusiophoretic phenomena, we believe the inclusion of finite double layer effects and imposing $\left|\frac{D_{DP}}{D_s}\right| \lesssim 1$ is likely be more reflective of experimental trends.

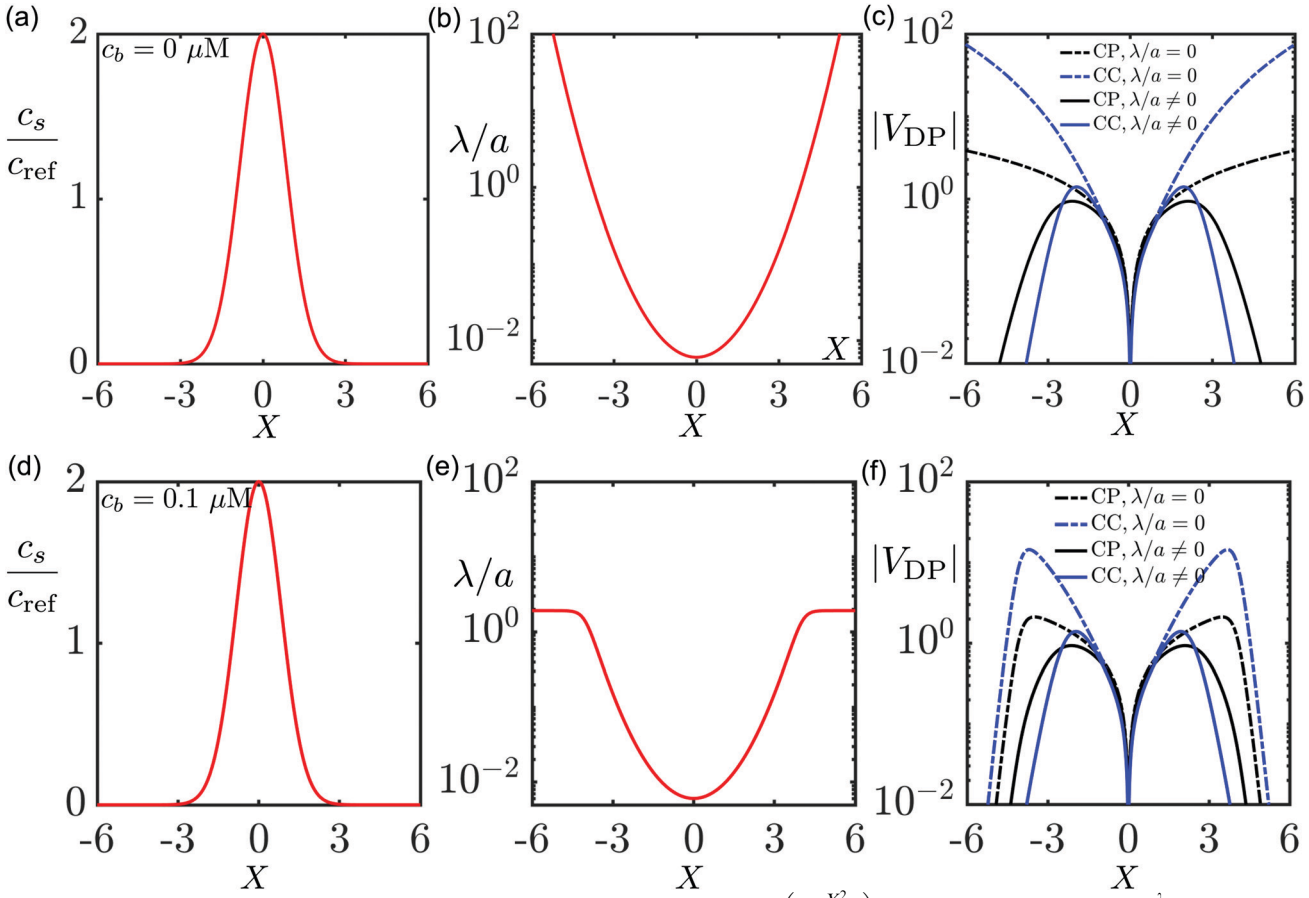

Fig. 4 Diffusiophoretic response to the spread of a Gaussian solute. (a) $c_s(X,\tau) = \frac{c_0}{\sqrt{1+4\tau}}\exp\left(-\frac{X^2}{1+4\tau}\right)$ for $\tau = 0.1$ and $c_0 = 11.8$ mM. (b) $\frac{\lambda}{a}$ estimated based on $c_s(X,0.1)$ and $c_0 = 11.8$ mM. (c) Prediction of the dimensionless diffusiophoretic velocity $\mathbf{v}_{DP}$ by using eqn (11) for different models. The models without the effect of finite double layer thickness $\left(\frac{\lambda}{a} = 0\right)$ predict a monotonically increasing velocity profile even in the region where the electrolyte concentration gradients are negligible. The models with the effect of finite double layer thickness $\left(\frac{\lambda}{a} \neq 0\right)$ predict that the velocity drops to zero for large X. (d) We modify the problem by adding a background solute concentration such that $c_s(X,\tau) = \frac{c_0}{\sqrt{1+4\tau}}\exp\left(-\frac{X^2}{1+4\tau}\right) + c_b$ for $\tau = 0.1$, $c_0 = 11.8$ mM and $c_b = 0.1$ μM. (e) $\frac{\lambda}{a}$ estimated based on $c_s(X,0.1)$, $c_0 = 11.8$ mM and $c_b = 0.1$ μM. (f) Prediction of the dimensionless diffusiophoretic velocity $\mathbf{v}_{DP}$ by using eqn (13) for different models. Physical parameters correspond to that an aqueous solution of NaCl where $\mathrm{Pe} = \frac{\varepsilon(k_B T/e)^2}{\mu D_s} = 0.28$. Curves are plotted assuming $a = 0.5$ μm, $\zeta_{ref} = -3$ and $c_{ref} = 5$ mM.

A variant of the above problem is to add a background chemical concentration since aqueous solutions usually possess ionic concentration of 0.1 μM, *i.e.*, the concentration of ions at pH = 7. We modify the concentration field by adding a constant background concentration as

$$c_s(X,\tau) = \frac{c_0}{\sqrt{1+4\tau}}\exp\left(-\frac{X^2}{1+4\tau}\right) + c_b, \qquad (12)$$

where c_b is the background concentration. By using eqn (12) to evaluate $\frac{\partial}{\partial X}(\log c_s)$ and substituting in eqn (10), we obtain

$$V_{DP}(X,\tau) = -2\mathrm{Pe}\left(\frac{u_0(\zeta)}{1-\frac{\lambda}{a}\frac{u_1(\zeta,\mathrm{Pe})}{u_0(\zeta)}}\right)\left(\frac{c_s - c_b}{c_s}\right)\frac{X}{1+4\tau}. \qquad (13)$$

We plot the results for the same parameters used previously with $c_b = 0.1$ μM; see Fig. 4(d)–(f). Since for $X = O(10)$, $\frac{c_s - c_b}{c_s} \ll 1$, V_{DP} decreases for large values of X in all scenarios. However, even if the predictions agree qualitatively for all scenarios, they disagree quantitatively, which is what we focus on in the next section.

5 The dead-end pore geometry

We now focus on the dead-end pore geometry[12–14,22,23,35] to quantitatively investigate the differences between different models and to compare the model predictions with experiments. In this setup, a dead-end pore of length ℓ is initially filled with a solution of electrolyte and colloidal particles; see Fig. 5(a).

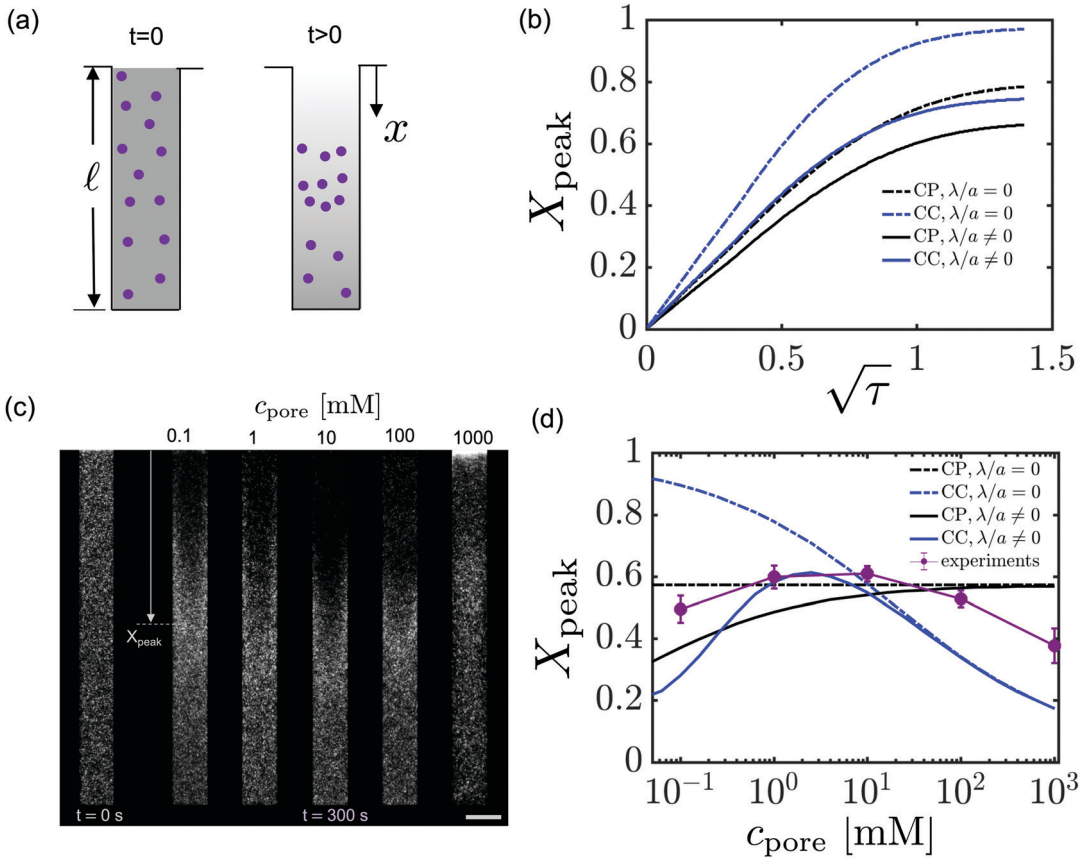

Fig. 5 The dead-end pore geometry. (a) Schematic of the problem setup. The dead-end pore of length ℓ is filled with a solution with electrolyte concentration $c_s = c_{pore}$ and the scaled particle concentration $n_p = 1$. Next, at $t = 0$, we bring the solution in the pore in contact with a reservoir where the electrolyte concentration $c_s = c_{bulk}$ and $n_p = 0$. Due to diffusiophoresis, the particles are compacted inside the pore. The value of $\frac{c_{bulk}}{c_{pore}} = \frac{1}{10}$ is kept constant across all experiments and models. (b) $n_p(X,\tau)$ is evaluated from different models obtained by numerically solving eqn (15). $X_{peak}(\tau)$ is obtained by finding the locations where n_p is maximum. X_{peak} *versus* $\sqrt{\tau}$ for different models and for c_{pore} = 1 mM. (c) Experimental snapshots at t = 300 s for a range of c_{pore} values and ℓ = 1 mm. Scale bar is 100 μm. The top of each image represents the mouth of the pore. At larger concentrations, the accumulation of colloids near the mouth of the pore is attributed to charge screening. (d) Comparison of the X_{peak} values between experiments and different models for a range of c_{pore} values at τ = 0.5. Physical parameters in the model correspond to that of an aqueous solution of NaCl where $\mathrm{Pe} = \frac{\varepsilon(k_B T/e)^2}{\mu D_s} = 0.28$. Curves for modeling trends are plotted assuming $c_{pore} = 10^{-1}$–10^3 mM, ℓ = 1 mm, $D_p = 2 \times 10^{-13}$ m^2 s^{-1}, a = 0.5 μm, c_{ref} = 5 mM and $\zeta_{ref} = -3$, *i.e.*, the parameter values consistent with the experiments. The experimental error bars are evaluated based on 3–4 independent experiments.

We assume that the configuration can be described through a one-dimensional model such that $\mathbf{v}_{fluid} = \mathbf{0}$. The initial concentration of electrolyte $c_s(0 \le x \le \ell, t = 0) = c_{pore}$ and particles $n_p(0 \le x \le \ell, t = 0) = 1$, where the particle concentration has been appropriately scaled. For $t > 0$, the solution inside the pore is brought in contact with a reservoir where $c_s(0,t) = c_{bulk}$ and $n_p(0,t) = 0$. Due to the diffusiophoretic motion of the particles, the particles get compacted inside the pore; see Fig. 5(a).

The electrolyte concentration can be described as[28]

$$c_s(X,\tau) = c_{bulk} + (c_{pore} - c_{bulk}) \sum_{k=0}^{\infty} \frac{2}{\lambda_k} \sin(\lambda_k X) \exp(-\lambda_k^2 \tau), \quad (14)$$

where $X = \frac{x}{\ell}$, $\tau = \frac{D_s t}{\ell^2}$ and $\lambda_k = (2k+1)\frac{\pi}{2}$. Next, we non-dimensionalize eqn (2) to get

$$\frac{\partial n_p}{\partial \tau} + \frac{\partial}{\partial X}(V_{DP} n_p) = \frac{D_p}{D_s} \frac{\partial n_p}{\partial X^2}, \quad (15)$$

where $V_{DP} = \mathrm{Pe}\left(\frac{u_0(\zeta)}{1 - \frac{\lambda}{a}\frac{u_1(\zeta,\mathrm{Pe})}{u_0(\zeta)}}\right)\frac{\partial}{\partial X}(\log c_s)$. We evaluate $\frac{\partial}{\partial X}(\log c_s)$ using eqn (14) and we numerically integrate eqn (15) using the method of lines and an implicit scheme with $n_p(X,0) = 1$, $n_p(0,\tau) = 0$ and $\left.\frac{\partial n_p}{\partial X}\right|_{X=1} = 0$. We utilized a grid with spacing $\delta X = 2.5 \times 10^{-3}$ and a time step $\delta\tau = 10^{-3}$. The values of physical parameters used are $c_{pore} = 10^{-1}$–10^3 mM, $c_{bulk} = \frac{c_{pore}}{10}$, ℓ = 1 mm, $D_p = 2 \times 10^{-13}$ m^2 s^{-1}, a = 0.5 μm, c_{ref} = 5 mM and $\zeta_{ref} = -3$. The remaining physical parameters are the same as that of an aqueous NaCl solution (provided earlier).

Next, we focus on the predictions of $n_p(X,\tau)$ obtained by integrating eqn (15). For each τ, we define the location $X_{peak}(\tau)$ as the location where n_p is maximum.[22] The effect of different boundary conditions and $\frac{\lambda}{a}$ models is provided in Fig. 5(b). Since the motion of particles is diffusive, X_{peak} *versus* $\sqrt{\tau}$ is linear for $\tau \lesssim 1$ and for all models; see Fig. 5(b).[22] However, for longer times, finite pore-size effects become significant and the X_{peak} profiles start to deviate from the linear behavior.[22] We note there are quantitative differences between the models.

We use a dead-end pore geometry (Fig. 5(a)) to perform compaction experiments[22] with polystyrene (PS; Invitrogen) particles of diameter 1 μm with volume fraction 2.6×10^{-4} in NaCl solution. Microfluidic channels are prepared by standard soft lithography, and the width, height, and the length of the main channel and the pores, respectively, are W = 750 μm, H = 150 μm and L = 5 cm, and w = 100 μm, h = 50 μm and ℓ = 1 mm.[23] As described in Fig. 5(a), we initially fill the pores with PS particles suspended in NaCl solution of concentration c_{pore}. Next, we introduce an air bubble into the main channel at a volumetric flow rate of 350 μL h^{-1}, which is followed by the second NaCl solution of concentration c_{bulk} (without particles). Once the two solutions come in contact with each other, the mean flow rate is reduced to 20 μL h^{-1}, corresponding to a mean flow speed $\langle u \rangle$ = 50 μm s^{-1} (syringe pump; Harvard Apparatus). Every experiment is repeated 3–4 times to gain confidence in the quantitative measurements. We vary $c_{pore} = 10^{-1}$, 1, 10^1, 10^2, 10^3 mM and fix $c_{bulk} = \frac{c_{pore}}{10}$. By fixing the concentration ratio for different experiments, we examine the role of ion concentrations on D_{DP} of PS particles while keeping the form of $\nabla \log c_s$ identical for all experiments; see eqn (14). We note that since $c_{bulk} = \frac{c_{pore}}{10}$, the lowest electrolyte concentration utilized in the experiment is 10^{-2} mM. Furthermore, since $c_{bulk} \leq c_s(x,t) \leq c_{pore}$, a background ion concentration of 0.1 μM, such as in eqn (12) and (13), is unlikely to significantly influence our dead-end pore analysis.

We obtain fluorescent images with an inverted microscope (Leica DMI4000B) and analyze the peak positions X_{peak} at t = 300 s (see Appendix). Fig. 5(c) shows fluorescent images of the dead-end pores from experiments for different c_{pore}. First, we note that the diffusiophoretic motion does result in compaction of colloidal particles; see Fig. 5(c). However, X_{peak} is dependent on the value of c_{pore}. If D_{DP} was independent of c_s, the microscopic images would have been identical across the entire range of c_{pore}. Clearly, this is not the case.

We now compare the predictions from different models with the experimental data; see Fig. 5(d). We find that the predicted trends for X_{peak} from different models are similar to that of D_{DP}; see Fig. 2. However, the quantitative differences between the models are smaller since the dependence of X_{peak} with D_{DP} is sub-linear.[22,35] The experimental analysis of X_{peak} with c_{pore} shows a maximum, similar to the model with the CC boundary condition with finite $\frac{\lambda}{a}$. Since the polystyrene particles employed in experiments are latex colloids,[37] the charge regulation boundary is the most appropriate, *i.e.*, the boundary condition which is a combination of the CP and the CC boundary conditions. Therefore, the decrease in the experimental X_{peak} values is less drastic as compared to the CC model. Finally, we also note that the maximum in X_{peak} is for the concentrations of $O(1)$ mM (note that $c(X,\tau) \leq c_{pore}$), consistent with our model. We acknowledge that there are quantitative differences between the experimental values and the model predictions, especially in predicting the distribution of particle concentration; see Fig. 7(c) in the Appendix. The disagreements arise due to the diffusioosmosis from the channel walls.[12,23] Another source of error is the charge screening effect at high salinity conditions due to which some particles stick to the wall (see Appendix), an effect that is not captured in the model. Finally, there are convection effects near the mouth of the pore,[38] which are currently ignored in the analysis. Nonetheless, our experimental results show that D_{DP} is not constant and possesses a maximum with c_s.

6 Conclusions

We conclude that diffusiophoretic mobility varies significantly with the electrolyte concentration for typical experimental conditions. For dilute electrolytes, the diffusiophoretic mobility decreases due to finite double layer effects. For concentrated electrolytes, the mobility decreases due to charge screening. Therefore, we observe a maximum in diffusiophoretic mobility for electrolyte concentrations around a few mM. Furthermore, we show that diffusiophoretic mobility is typically smaller than the solute ambipolar diffusivity. We also show that incorporating the finite double layer thickness effects, the diffusiophoretic response to the spread of a Gaussian solute does not yield a ballistic motion. Moreover, for the dead-end pore geometry, we find that experiments also predict a maximum in the diffusiophoretic mobility with ion concentration, in agreement with our modeling predictions.

Looking forward, our results suggest that to achieve maximum diffusiophoretic transport rates in experiments, it is advisable to have $c_s = O(1) - O(10)$ mM, at least for $a = O(1)$ μm. Furthermore, the condition $\left|\frac{D_{DP}}{D_s}\right| \lesssim 1$ will help identify the physical scenarios where diffusiophoresis is likely to be significant. Moreover, a precise measurement of diffusiophoretic mobilities might assist in classifying the surface chemistry of the particles, *i.e.*, constant potential, constant charge or charge regulation.

We recently estimated the leading-order diffusiophoretic mobility, *i.e.*, $u_0(\zeta)$ in eqn (5), for a mixture of multivalent electrolytes.[20] Our results here motivate the need to evaluate D_{DP} for a mixture of electrolytes because the values of $u_1(\zeta,Pe)$ and $\frac{\lambda}{a}$ will need to be appropriately modified. Since electrolytic diffusiophoresis has potential applications in delivery or extraction of particles to dead-end pore,[13,14] colloidal focusing or trapping[15–17] and lab-on-a-chip devices,[11,12] our results emphasize the need to consider the finite double layer effects in regions with low ion concentrations.

Conflicts of interest

There are no conflicts to declare.

Appendix: description of $u_1(\zeta,\mathrm{Pe})$

To complete the description of D_{DP} in eqn (5), $u_1(\zeta,\mathrm{Pe})$ is evaluated as

$$u_1(\zeta,\mathrm{Pe}) = \frac{1}{2}\left(F_0 + \beta F_1 + \frac{\mathrm{Pe}}{2}\left(F_2 + \beta(F_3+F_5) + \beta^2 F_4\right)\right), \quad (16)$$

where for $\zeta > 0$, $F_n(\zeta)$ are evaluated numerically as

$$F_0(\zeta) = \frac{1}{3}\int_0^\infty \left[y^3 \sinh\phi_0 \frac{\mathrm{d}\phi_0}{\mathrm{d}y} - 3y^2 \sinh\phi_0 \frac{\mathrm{d}\phi_1}{\mathrm{d}y} + y^2 f_0 \frac{\mathrm{d}\phi_0}{\mathrm{d}y}\right]\mathrm{d}y, \quad (17)$$

$$F_1(\zeta) = \frac{1}{3}\int_0^\infty \left[y^3 \cosh\phi_0 \frac{\mathrm{d}\phi_0}{\mathrm{d}y} - 3y^2 \cosh\phi_0 \frac{\mathrm{d}\phi_1}{\mathrm{d}y} + y^2 f_1 \frac{\mathrm{d}\phi_0}{\mathrm{d}y}\right]\mathrm{d}y, \quad (18)$$

$$F_n(\zeta) = \frac{1}{3}\int_0^\infty y^2 f_n \frac{\mathrm{d}\phi_0}{\mathrm{d}y}\mathrm{d}y, \quad (n = 2,3,4,5) \quad (19)$$

$$f_0(y) = -3\phi_1 \cosh\phi_0 + 6\left(\sinh\left(\frac{\zeta}{2}+\phi_0\right) - \sinh\phi_0\right), \quad (20)$$

$$f_1(y) = -3\phi_1 \sinh\phi_0 + 6\left(\cosh\left(\frac{\zeta}{2}+\phi_0\right) - \cosh\phi_0\right), \quad (21)$$

$$\begin{aligned} f_2(y) &= -\mathrm{e}^{\phi_0}\int_0^\infty I_0(y_1)\mathrm{e}^{\phi_0(y_1)}\sinh\left(\frac{\phi_0(y_1)}{2}\right)\mathrm{d}y_1 \\ &\quad - \mathrm{e}^{-\phi_0}\int_0^\infty I_0(y_1)\mathrm{e}^{-\phi_0(y_1)}\sinh\left(\frac{\phi_0(y_1)}{2}\right)\mathrm{d}y_1, \end{aligned} \quad (22)$$

$$\begin{aligned} f_3(y) &= -\mathrm{e}^{\phi_0}\int_0^\infty I_0(y_1)\mathrm{e}^{\phi_0(y_1)}\sinh\left(\frac{\phi_0(y_1)}{2}\right)\mathrm{d}y_1 \\ &\quad + \mathrm{e}^{-\phi_0}\int_0^\infty I_0(y_1)\mathrm{e}^{-\phi_0(y_1)}\sinh\left(\frac{\phi_0(y_1)}{2}\right)\mathrm{d}y_1 \end{aligned} \quad (23)$$

$$\begin{aligned} f_4(y) &= -\mathrm{e}^{\phi_0}\int_0^\infty I_1(y_1)\mathrm{e}^{\phi_0(y_1)}\sinh\left(\frac{\phi_0(y_1)}{2}\right)\mathrm{d}y_1 \\ &\quad + \mathrm{e}^{-\phi_0}\int_0^\infty I_1(y_1)\mathrm{e}^{-\phi_0(y_1)}\sinh\left(\frac{\phi_0(y_1)}{2}\right)\mathrm{d}y_1, \end{aligned} \quad (24)$$

$$\begin{aligned} f_5(y) &= -\mathrm{e}^{\phi_0}\int_0^\infty I_1(y_1)\mathrm{e}^{\phi_0(y_1)}\sinh\left(\frac{\phi_0(y_1)}{2}\right)\mathrm{d}y_1 \\ &\quad - \mathrm{e}^{-\phi_0}\int_0^\infty I_1(y_1)\mathrm{e}^{-\phi_0(y_1)}\sinh\left(\frac{\phi_0(y_1)}{2}\right)\mathrm{d}y_1 \end{aligned} \quad (25)$$

$$I_0(y) = 12\left[y\log\left(1-\gamma^2\right) - \int_0^y \log\left(1-\gamma^2\mathrm{e}^{-2y_1}\right)\mathrm{d}y_1\right], \quad (26)$$

$$I_1(y) = -24\left[y\tanh^{-1}\gamma - \int_0^y \tanh^{-1}(\gamma\mathrm{e}^{-y_1})\mathrm{d}y_1\right], \quad (27)$$

where $\gamma = \tanh\left(\frac{\zeta}{4}\right)$, $\tanh\left(\frac{\phi_0(y)}{4}\right) = \gamma e^{-y}$ and $\phi_1(y) = \frac{2\gamma\mathrm{e}^{-y}}{1-\gamma^2\mathrm{e}^{-2y}}\left[\gamma^2\left(1-\mathrm{e}^{-2y}\right) - 2y\right]$. To evaluate $F_n(\zeta)$ for $\zeta < 0$, one can exploit the relation $F_n(-\zeta) = (-1)^n F_n(\zeta)$. We refer the readers to ref. 3 for the details of the derivation.

Appendix: D_{DP} for constant potential boundary condition

We repeat the analysis presented in Fig. 3 but with the constant potential boundary condition. The results are presented in Fig. 6. The analysis further underscores that $\left|\frac{D_{\mathrm{DP}}}{D_s}\right| \lesssim 1$.

Appendix: analysis of experiments

To obtain the X_{peak} values (reported in Fig. 5(d)), we first evaluate the width-averaged intensity along the length of the pore; see Fig. 7(a). We conduct every experiment 3–4 times and report the average values. Next, X_{peak} is determined as the local maximum that appears after the boundary of exclusion zones; see Fig. 7(b). We note that when $c_{\mathrm{pore}} = 1$ M, the axial variation in intensity is smaller because particles get attached to the wall due to charge screening; see Fig. 5(c) and 7(b). We also provide a direct comparison of the experimentally obtained particle concentration distribution with the numerical results obtained by solving eqn (15) for the CC boundary condition and $\frac{\lambda}{a} \neq 0$; see Fig. 7(c).

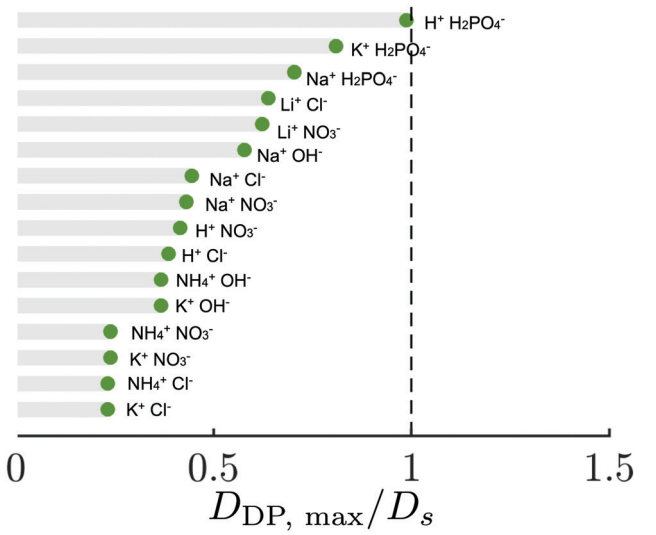

Fig. 6 Summary of maximum $\frac{D_{\mathrm{DP}}}{D_s}$ values for 16 different electrolytes based on the constant potential boundary condition and while including finite double layer effects. We adjusted the sign of the zeta potential such that $\beta\zeta > 0$ to ensure that the electrophoretic term and the chemiphoretic term are additive; see eqn (6). We assume $\zeta_{\mathrm{ref}} = \pm 3$ (corresponding to ± 75 mV) at $a = 0.5$ μm and $c_{\mathrm{ref}} = 5$ mM. The diffusivity values for cations and anions are taken from ref. 2.

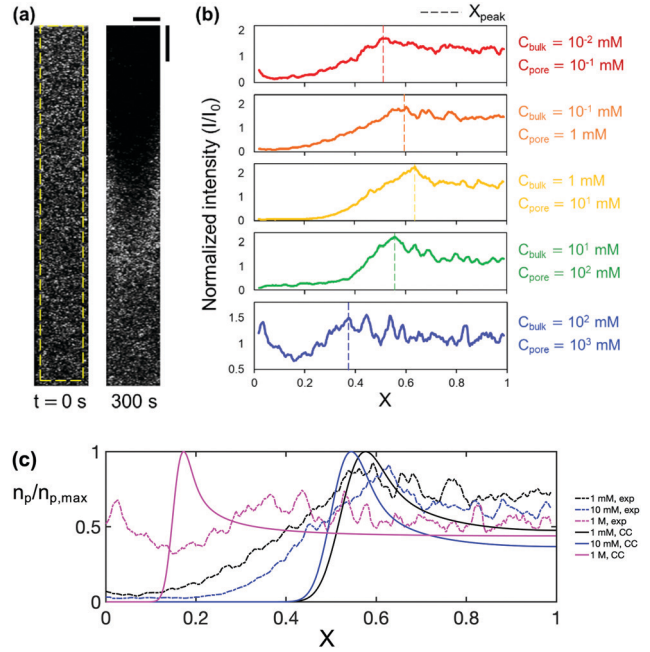

Fig. 7 Procedure to evaluate X_{peak} at t = 300 s from the intensity plots along X. (a) We measure the gray values along the pore using the region of interest (ROI, 80 μm X 990 μm), *i.e.*, the region indicated with the dashed box. The top side of ROI is aligned with the inlet of the pore, and the other three sides are 10 μm away from the pore walls. The images are shown for c_{bulk} = 1 mM and c_{pore} = 10 mM. The horizontal and vertical scale bars are, respectively, 50 μm and 100 μm. (b) Typical intensity plots for a range of c_{pore} values at t = 300 s. The peak location X_{peak} is defined as the local maximum that appears after the boundary of exclusion zones. The presented plots are averaged values from 3–4 independent experiments (corresponding to 11–15 pores). A moving average of period 10 is applied to reduce the noise in the intensity data. (c) Comparison of $\frac{n_p}{n_{p,max}}(x, 300\ s)$. The experimental data does not reach unity because of the moving average. The numerical data is obtained from the constant charge model while including the finite double layer thickness effects.

Acknowledgements

We thank the Andlinger Center for Energy and the Environment at Princeton University and the NSF grant CBET-1702693 for financial support for our research. We thank Prof. Robert K. Prud'homme for helpful discussions. We also thank the two anonymous referees for their insightful comments.

References

1 B. Derjaguin, G. Sidorenkov, E. Zubashchenkov and E. Kiseleva, *Kolloidn. Zh.*, 1947, **9**, 335–347.
2 D. Velegol, A. Garg, R. Guha, A. Kar and M. Kumar, *Soft Matter*, 2016, **12**, 4686–4703.
3 D. Prieve, J. Anderson, J. Ebel and M. Lowell, *J. Fluid Mech.*, 1984, **148**, 247–269.
4 J. L. Anderson, *Annu. Rev. Fluid Mech.*, 1989, **21**, 61–99.
5 Y. Pawar, Y. E. Solomentsev and J. L. Anderson, *J. Colloid Interface Sci.*, 1993, **155**, 488–498.
6 D. C. Prieve and R. Roman, *J. Chem. Soc., Faraday Trans. 2*, 1987, **83**, 1287–1306.
7 J. Palacci, C. Cottin-Bizonne, C. Ybert and L. Bocquet, *Soft Matter*, 2012, **8**, 980–994.
8 J. Palacci, B. Abécassis, C. Cottin-Bizonne, C. Ybert and L. Bocquet, *Phys. Rev. Lett.*, 2010, **104**, 138302.
9 A. E. Frankel and A. S. Khair, *Phys. Rev. E: Stat., Nonlinear, Soft Matter Phys.*, 2014, **90**, 013030.
10 A. Banerjee, I. Williams, R. N. Azevedo, M. E. Helgeson and T. M. Squires, *Proc. Natl. Acad. Sci. U. S. A.*, 2016, **113**, 8612–8617.
11 S. Shin, O. Shardt, P. B. Warren and H. A. Stone, *Nat. Commun.*, 2017, **8**, 15181.
12 S. Shin, J. T. Ault, J. Feng, P. B. Warren and H. A. Stone, *Adv. Mater.*, 2017, **29**, 1701516.
13 A. Kar, T.-Y. Chiang, I. Ortiz Rivera, A. Sen and D. Velegol, *ACS Nano*, 2015, **9**, 746–753.
14 S. Shin, E. Um, B. Sabass, J. T. Ault, M. Rahimi, P. B. Warren and H. A. Stone, *Proc. Natl. Acad. Sci. U. S. A.*, 2016, **113**, 257–261.
15 N. Shi, R. Nery-Azevedo, A. I. Abdel-Fattah and T. M. Squires, *Phys. Rev. Lett.*, 2016, **117**, 258001.
16 B. Abécassis, C. Cottin-Bizonne, C. Ybert, A. Ajdari and L. Bocquet, *Nat. Mater.*, 2008, **7**, 785.
17 S. Shin, J. T. Ault, K. Toda-Peters and A. Q. Shen, *Phys. Rev. Fluids*, 2020, **5**, 024304.
18 R. Nery-Azevedo, A. Banerjee and T. M. Squires, *Langmuir*, 2017, **33**, 9694–9702.
19 D. C. Prieve, S. M. Malone, A. S. Khair, R. F. Stout and M. Y. Kanj, *Proc. Natl. Acad. Sci. U. S. A.*, 2019, **116**, 18257–18262.
20 A. Gupta, B. Rallabandi and H. A. Stone, *Phys. Rev. Fluids*, 2019, **4**, 043702.
21 A. Gupta and H. A. Stone, *Langmuir*, 2018, **34**, 11971–11985.
22 J. L. Wilson, S. Shim, Y. E. Yu, A. Gupta and H. A. Stone, *Langmuir*, 2020, **36**, 7014–7020.
23 A. Gupta, S. Shim, L. Issah, C. McKenzie and H. A. Stone, *Soft Matter*, 2019, **15**, 9965–9973.
24 T.-Y. Chiang and D. Velegol, *J. Colloid Interface Sci.*, 2014, **424**, 120–123.
25 H. C. Chu, S. Garoff, R. D. Tilton and A. S. Khair, *Soft Matter*, 2020, **16**, 238–246.
26 F. Raynal, M. Bourgoin, C. Cottin-Bizonne, C. Ybert and R. Volk, *J. Fluid Mech.*, 2018, **847**, 228–243.
27 F. Raynal and R. Volk, *J. Fluid Mech.*, 2019, **876**, 818–829.
28 W. M. Deen, *Analysis of Transport Phenomena*, Oxford University Press, New York, 2012.
29 J. Lyklema, *Fundamentals of Interface and Colloid Science*, Academic Press, 1995, vol. 2.
30 B. J. Kirby and E. F. Hasselbrink Jr, *Electrophoresis*, 2004, **25**, 187–202.
31 B. W. Ninham and V. A. Parsegian, *J. Theor. Biol.*, 1971, **31**, 405–428.
32 D. C. Prieve and E. Ruckenstein, *J. Theor. Biol.*, 1976, **56**, 205–228.

33 J. Krozel and D. Saville, *J. Colloid Interface Sci.*, 1992, **150**, 365–373.
34 T. Markovich, D. Andelman and R. Podgornik, *EPL*, 2016, **113**, 26004.
35 J. T. Ault, P. B. Warren, S. Shin and H. A. Stone, *Soft Matter*, 2017, **13**, 9015–9023.
36 R. J. Hunter, *Zeta Potential in Colloid Science: Principles and Applications*, Academic Press, 2013, vol. 2.
37 T. W. Healy and L. R. White, *Adv. Colloid Interface Sci.*, 1978, **9**, 303–345.
38 S. Battat, J. T. Ault, S. Shin, S. Khodaparast and H. A. Stone, *Soft Matter*, 2019, **15**, 3879–3885.